chemosensors

MDPI

Article

Enhanced Oxygen Vacancies in Ni-Doped SnO_2 Nanorods via Aerosol-Assisted Chemical Vapor Deposition for Low-Concentration Hydrogen Detection

Peng Chen [1], Xin Zhang [1], Jiacheng Liu [1], Xu Li [2], Min Chen [1] and Qingji Wang [1,*]

[1] College of Information and Communication Engineering, Hainan University, Haikou 570228, China; chenmin@hainanu.edu.cn (M.C.)
[2] School of Chemistry and Chemical Engineering, Hainan Normal University, Haikou 571158, China; lixu@hainnu.edu.cn
* Correspondence: wangqingji@hainanu.edu.cn

Abstract

Hydrogen is a clean energy carrier essential for carbon neutrality, but its invisible and odorless nature poses significant safety risks, particularly during low-concentration leaks. Although metal oxide semiconductor (MOS) sensors offer fast response and high sensitivity, their ability to detect ppb-level hydrogen remains limited. In this work, we present a high-performance hydrogen gas sensor based on nickel-doped tin dioxide (Ni-SnO_2) nanorods, directly grown on planar electrodes via aerosol-assisted chemical vapor deposition (AACVD). By optimizing the Ni doping ratio and nanorod morphology, the 3 wt% Ni-SnO_2 sensor achieves a low detection limit of 100 ppb for H_2, demonstrating promising potential for low-concentration hydrogen detection. Moreover, the sensor exhibits outstanding selectivity, with a response to 100 ppm H_2 nearly six times higher than that to the next most responsive interfering gas (NH_3). Comprehensive XPS and Raman analyses reveal that Ni doping introduces abundant oxygen vacancies and lattice defects, which are the key origins of the enhanced sensing performance. Notably, the 3 wt% Ni-SnO_2 sensor strikes an optimal balance between lattice defects and structural stability, delivering both high sensitivity and good moisture resistance with minimal baseline drift over weeks of operation. This work establishes a facile and scalable AACVD strategy for engineering defect-rich SnO_2 nanostructures, enabling sub-ppm hydrogen detection with high selectivity and long-term stability—addressing a critical gap in practical hydrogen safety monitoring.

Keywords: Ni doping; SnO_2; nanorods; AACVD; H_2 sensor

Received: 18 May 2026
Revised: 8 July 2026
Accepted: 10 July 2026
Published: 15 July 2026

1. Introduction

Against the backdrop of the escalating global energy crisis, hydrogen has emerged as a carbon-free and high-performance energy carrier, playing a pivotal role in energy-structure transformation [1]. However, its colorless and odorless nature makes leakage detection by human senses virtually impossible. As hydrogen energy becomes more widely adopted, even low-concentration leaks pose serious risks to life and property safety. Therefore, the development of high-performance hydrogen sensors that enable rapid and accurate detection is a pivotal technological driver—not only for the safe utilization of hydrogen energy, but also as a critical enabler of the global transition to clean energy. Currently, hydrogen detection methods have been developed based on various principles, including

gas chromatography for precision analysis, optical sensor for stable performance, electrochemical sensors for good selectivity and semiconductor sensor for high sensitivity [2–5]. Among these technological approaches, MOS sensors have shown unique application in both industrial safety and daily scenarios, owing to their advantages including superior sensitivity, trace-level detection, cost efficiency and simple integration [6,7].

The basic working mechanism of MOS sensors involves surface adsorption and reactions triggered by target gas exposure, leading to changes in the material's electrical resistance. Leveraging this phenomenon, researchers have extensively employed a variety of MOS sensing-materials and development of resistive gas sensors. Typical sensing materials include SnO_2 [8], ZnO [9], WO_3 [10] and In_2O_3 [11]. As a typical n-type MOS material, SnO_2 exhibits key advantages such as high carrier mobility, excellent chemical stability, facile property tunability and favorable economic attributes [12]. Consequently, it has been widely adopted in gas sensors. Beyond these intrinsic properties, its sensing performance is also profoundly influenced by material morphology. Various SnO_2 nanostructures—nanowires [13], nanorods [14], nanoflowers [15], and nanosheets [16]—have been applied for gas sensing, with each morphology yielding distinct performance: nanowires gave a response of 5.7 to 1000 ppm H_2 (150 °C, LOD 100 ppm); Pd-decorated nanorods achieved 39.3 to 10 ppm H_2 (80 °C, LOD 0.5 ppm); SnS_2/SnO_2 nanoflowers exhibited 83.9% to 50 ppm NO_2 (room temperature, LOD 10 ppm); and C_3N_4/SnO_2 nanosheets delivered 8.8 to 10 ppm formaldehyde (260 °C, LOD 0.1 ppm). Among various nanostructures, nanorods provide efficient axial carrier transport due to their one-dimensional single-crystal nature, thus significantly enhancing the response speed of electrical signals. Additionally, the morphological uniformity and structural stability of nanorods enables this synergistic enhancement for superior performance, response speed and good selectivity. The primary drawback posed by high detection limits has been a key motivation for advancing research into high-performance sensing alternatives. The challenge of low detection limits has driven the development of several sensitization strategies, including noble metal functionalization, oxide compositing, and elemental doping. Elemental doping improves sensitivity and low detection limits by generating abundant lattice defects via electronic structure modulation [17], which promotes oxygen molecule adsorption and dissociation [18]. Pt functionalization [19], SnO_2/ZnO compositing [20], and Ni doping [21] have been adopted, yielding notably improved responses toward various target gases with detection limits down to ppb levels. Oxide doping has been demonstrated to significantly optimize the interplay between electronic structure and surface properties in SnO_2. The primary strategy involves constructing heterogeneous interfaces and, more critically, creating abundant oxygen vacancies, with the vacancies representing highly active sites that enhance electron transfer efficiency and facilitate gas adsorption [22,23]. Oxide doping is key to achieving high sensitivity and superior selectivity of sensors by the interplay of defect engineering and electronic modulation. The ionic radius of Ni, similar to that of Sn, allows its easy incorporation into the SnO_2 crystal lattice. This incorporation effectively regulates the band gap and introduces defects, positioning Ni as an effective dopant for enhancing the performance of SnO_2 gas sensors [24]. To date, SnO_2-based gas sensors have been successfully prepared via diverse techniques such as hydrothermal synthesis [25], electrospinning [26], and aerosol-assisted chemical vapor deposition (AACVD) [27]. Owing to the ability to directly deposit films onto electrodes, AACVD has garnered significant attention in sensor fabrication with a simple process and high stability. The value of AACVD technology lies in its capacity to precisely control reaction conditions and chemical stoichiometry, thus enabling the synthesis of thin films with tailored morphologies and structures. This capability facilitates innovation not only in film preparation but also in the broader design of functional materials.

In this study, AACVD was employed to synthesize Ni-doped SnO_2 nanorods in situ on planar electrodes, thereby fabricating a high-performance H_2 sensor. The sensing performance reveals that the 3 wt% Ni-SnO_2 sensor exhibited a capability of detecting at the 100 ppb level and high selectivity for hydrogen (S_{H2}/S_{NH3} = 5.7). To elucidate the mechanism behind performance enhancement, comprehensive characterization was performed to probe morphological, structural, and defect changes in the material induced by Ni doping. The results demonstrate that Ni doping optimizes the oxygen vacancies, thereby enhancing its sensing response. This work confirms that AACVD-mediated Ni doping is a viable strategy to dramatically improve the H_2 sensing capabilities of SnO_2.

2. Materials and Methods

2.1. Synthesis of SnO_2 Seed Layers

Crystalline tin tetrachloride ($SnCl_4 \cdot 5H_2O$, ≥99%), nickel(II) chloride hexahydrate ($NiCl_2 \cdot 6H_2O$, ≥99%) and L-malic acid ($C_4H_6O_5$, ≥98%) were obtained from Aladdin (Shanghai, China). The SnO_2 seed layer was fabricated using AACVD. The SnO_2 nanorods were then grown on the seed layer, forming directly onto the interdigitated electrode (Figure 1). A solution of tin tetrachloride (10 mmol in 20 mL of deionized water) was prepared, followed by the addition of 0.4 mmol of L-malic acid and continuous stirring for 15 min to obtain a homogeneous precursor solution. This precursor solution was transferred into a 500 mL flask and subsequently loaded into the AACVD system. A forked electrode was positioned horizontally in the central zone of the tube furnace. To enhance crystallinity and eliminate organic residues from the seed layer, the as-deposited layer was annealed at 500 °C for 2 h following the 30 min deposition at 300 °C.

Figure 1. Schematic illustration of the preparation of Ni-SnO_2 films via the AACVD.

2.2. Synthesis of SnO_2 Nanorods

The detailed procedure for a typical preparation of 3 wt% Ni-doped SnO_2 is as follows: A solution of tin tetrachloride (4 mmol in 20 mL deionized water) was prepared, to which 0.075 g of $NiCl_2 \cdot 6H_2O$ and 3.2 mmol of L-malic acid were added. The mixture was continuously stirred for 15 min to obtain a homogeneous precursor solution. The resulting solution was transferred to the ultrasonic atomizer of the AACVD system, and the generated aerosol was delivered to a pre-cleaned substrate using a carrier gas. The deposition was conducted at 500 °C for 30 min. During this process, the precursor decomposed and crystallized in the thermal field, leading to the formation of nanostructures on the substrate. Finally, the nanorods were annealed at 500 °C for 2 h. Using the same procedure, pure SnO_2 and Ni-SnO_2 composites containing 1 wt% and 5 wt% Ni were fabricated by using different amounts of $NiCl_2 \cdot 6H_2O$ (0 g, 0.0246 g, and 0.128 g, respectively).

2.3. Characterization

A multi-technique characterization approach was employed to systematically investigate the prepared sensing materials, from their microstructure to surface chemistry. Surface morphology and nanostructure were observed using a scanning electron microscope (SEM; Gemini 360, Zeiss, Oberkochen, Germany); The crystallographic structure and lattice in-

formation were further analyzed by transmission electron microscopy (TEM; Talos F200X, Thermo Fisher Scientific, Waltham, MA, USA) operated at 200 kV in high-resolution TEM (HRTEM) mode. Phase identification was performed using an X-ray diffractometer (XRD; SmartLab SE, Rigaku Corporation, Tokyo, Japan) with Cu Kα_1 radiation (λ = 1.5406 Å) at 40 kV and 15 mA. Raman spectroscopy was employed to probe molecular vibrational modes and assess structural integrity. In addition, surface elemental composition and chemical states were characterized by X-ray photoelectron spectroscopy (XPS; ESCALAB QXi, Thermo Fisher Scientific, Cheshire, UK). Functional groups and chemical bonding information were identified using Fourier-transform infrared spectroscopy (FT-IR).

2.4. Gas Sensor Measurements

The sensing materials were grown on the forked electrode using the AACVD method. The electrodes coated with sensing materials were then wire-bonded onto the sensor base to facilitate subsequent testing. Prior to gas-sensing measurements, power was supplied to the heating resistor, and the sensor was aged in ambient air for 2 days. The forked electrode structure enables temperature modulation by varying the current through the Pt heating resistor. Gas-sensing performance was evaluated under static test conditions at 25 °C and 50% relative humidity (RH) in air. The test gases (CO_2, CO, H_2, CH_4, and NH_3) were obtained as certified standard gas mixtures with a volume fraction of 1%, supplied by Shanghai Weichuang Standard Gas Analysis Technology Co, Shanghai, China. Gas concentrations for sensing tests were dynamically configured using a two-cylinder dilution method. For example, to generate 100 ppm H_2, two 1 L cylinders were first filled with purified air using an air pump. One cylinder remained as a pure air reference, while 10 mL of the 1% H_2 standard gas was injected into the second cylinder, resulting in a final concentration of 100 ppm H_2 for sensor testing. The resistance of the sensor was recorded every second using a FLUKE digital multimeter to capture its sensing characteristics. The sensor response was measured through a sequential resistance recording procedure. Initially, the baseline resistance in clean air (Rair) is recorded. The sensor was exposed to test gas, and stabilized resistance (Rgas) was measured. The response (S) was calculated as: $S = (Rair/Rgas - 1) \times 100\%$. The response time was defined as the time to reach by 90% of the total resistance change upon gas exposure, and the recovery time as the time to achieve 90% resistance restoration after gas removal. In this work, the LOD is defined as the lowest H_2 concentration experimentally tested. For reference, the theoretical limit of detection (LOD) was calculated using the standard formula $LOD = 3 \times RMS/S$, where S is the slope of the calibration curve in its linear range, and RMS is the root-mean-square noise of the baseline.

3. Results and Discussion

3.1. Structural and Morphological Analysis

The structural properties of the Ni-SnO_2 nanorods were determined by XRD, with the results presented in Figure 2a. The diffraction pattern shows distinct peaks at 26.61°, 33.89°, 37.95°, and 51.78°, which can be assigned to the (110), (101), (200), and (211) crystallographic planes of rutile-structured SnO_2 (PDF #41-1445), thereby confirming the dominant presence of the SnO_2 phase. The sharp nature of all diffraction peaks indicates crystallinity [16]. Notably, the relative intensity of the (101), (211), and (301) peaks exhibits visible fluctuations with increasing Ni content, which could be attributed to the lattice strain and modification of the structure factor caused by Ni incorporation [28]. The enlarged view of the (101) diffraction peak in Figure 2b shows that this peak exhibits a systematic shift with increasing Ni doped content. This observation confirms that the introduction of Ni induces a contraction of the SnO_2 lattice constants, which may originate from lattice distortion

caused by the doping of Sn^{4+} ions (0.071 nm) with the smaller Ni^{2+} ions (0.069 nm), thereby effectively modulating the crystal structure and lattice parameters of SnO_2 [29].

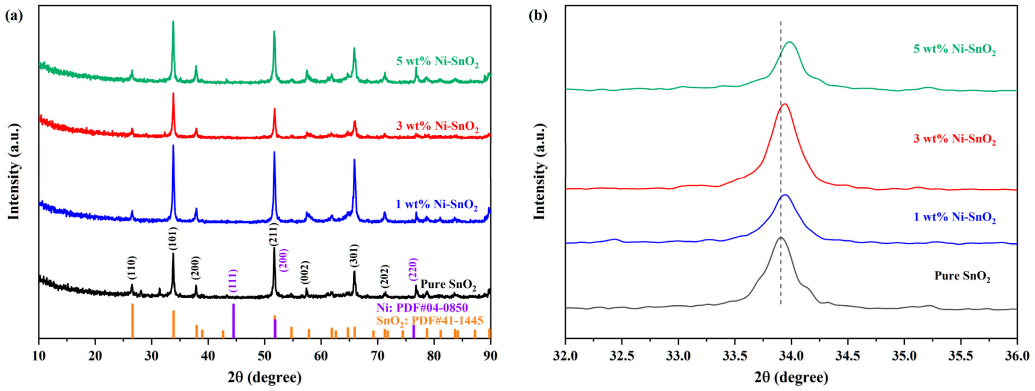

Figure 2. (**a**) XRD pattern of the sample; (**b**) enlarged view of peak (101).

The morphological characteristics of all samples grown in situ on Al_2O_3 substrates were systematically investigated using SEM. As illustrated in Figure 3, all samples successfully formed continuous thin films composed of two-dimensional nanorods. It is noteworthy that the geometric morphology and spatial arrangement of the nanorods showed no significant variation across different doping levels. This is mainly because Ni^{2+} has an ionic radius similar to that of Sn^{4+}, so the incorporation of Ni does not cause significant lattice distortion or alter the surface energies of different crystal planes, thereby preserving the original growth habit of the rod-like morphology. Statistical analysis of multiple SEM images yielded an average nanorod diameter of approximately 70 nm, indicating good size uniformity. The resulting interconnected structure significantly enlarges the accessible surface area while establishing efficient, continuous pathways for gas molecule diffusion and transport throughout the sensing layer. Such an optimized morphology is critical for accelerating gas response dynamics and amplifying the sensor's overall sensitivity [30]. SEM characterization reveals a highly uniform and continuous film surface, where the nanorods are evenly distributed. Cross-sectional analysis further corroborates the structural homogeneity, yielding a consistent film thickness of approximately 1.9 μm. This well-defined and reproducible microstructure is a direct result of the precise deposition control afforded by the AACVD technique. The AACVD technique facilitates the ordered growth of nanorods on the substrate through uniform precursor aerosolization and controlled thermal decomposition. Such structural homogeneity not only underscores the reliability of AACVD for fabricating nanostructures but also provides a promising platform for developing advanced gas sensors, ensuring excellent device-to-device consistency and reproducibility.

The microstructure of 3 wt% Ni-SnO_2 nanofilm was further analyzed by HRTEM. Figure 4a shows the overall morphology of the sample, revealing uniformly distributed nanorod-like structures with relatively smooth surfaces. However, continuous lattice fringes are difficult to resolve across the entire nanorod due to severe projection overlap and structural disorder inherently associated with the porous frameworks, lattice fringes in HRTEM are locally visible along the edges of the nanorods [31]. In Figure 4b, distinct lattice fringes can still be locally identified along the thinner edge or tail regions of the nanorods, where the sample thickness is minimized to reduce overlap effects. These visible fringes exhibit a spacing of 0.264 nm, which can be indexed to the (101) crystallographic plane of the rutile-structured SnO_2 phase (PDF #41-1445), attesting to its good structural quality. Combining the elemental distribution maps (Figure 4c–e) with the lattice fringe analysis, it can be seen that Ni is uniformly distributed within the SnO_2 nanorods. The relatively

weak Ni signal in the EDS mapping is due to the low doping concentration (3 wt%) and the homogeneous atomic-scale dispersion of Ni within the SnO_2 lattice, with no detectable Ni-rich aggregates. Quantitative EDS (Figure 4f) gives a Ni content of 1.82 wt%, slightly below the nominal 3 wt%, which may be ascribed to precursor transport loss during AACVD and surface enrichment of SnO_2 during crystallization. It should be noted that the atomic ratio of Sn:O slightly deviates from the ideal 1:2 stoichiometry, which is in consensus with the semi-quantitative nature of EDS for light elements (such as O) and the existence of doping-induced oxygen vacancies. Although the local nature of the lattice fringes indicates a degree of structural disorder or disordered porous features within the nanorods, the bulk single-phase characteristic verified by XRD confirms that the framework maintains the basic rutile SnO_2 structure. This configuration provides a suitable combination of crystalline paths and disordered defect-rich regions, which can serve as surface active sites to benefit the gas-sensing performance.

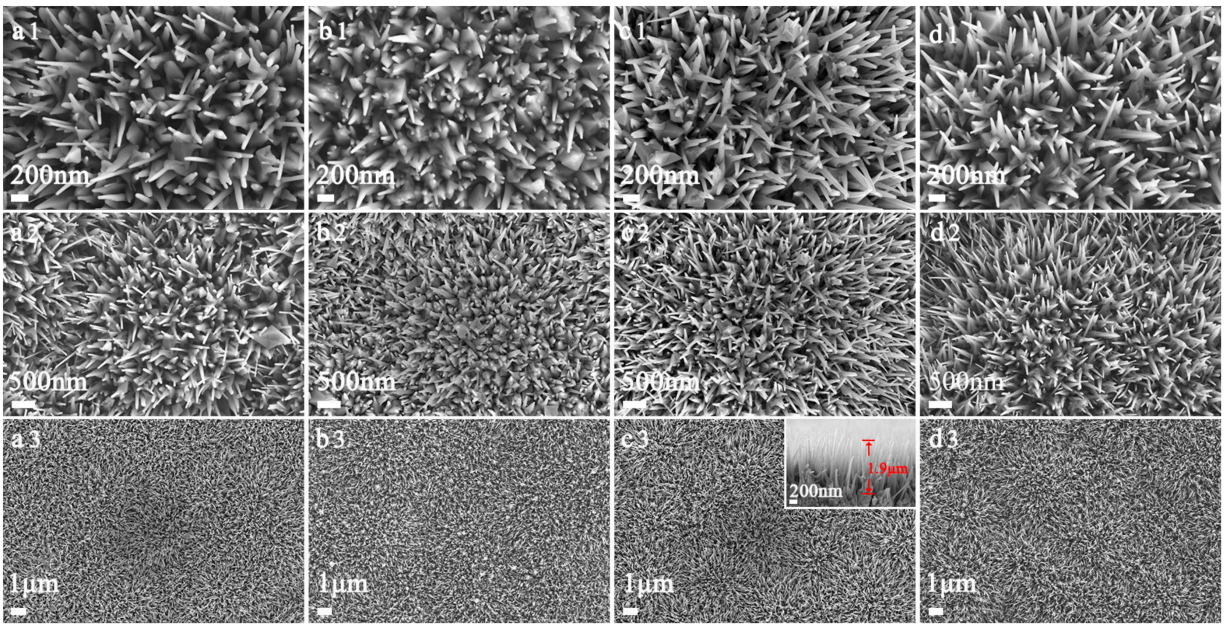

Figure 3. SEM images: (**a1**–**a3**) SnO_2; (**b1**–**b3**) 1 wt% Ni-SnO_2; (**c1**–**c3**) 3 wt% Ni-SnO_2; (**d1**–**d3**) 5 wt% Ni-SnO_2.

The surface chemistry and electronic configuration were investigated using XPS. All XPS binding energies were calibrated against the adventitious carbon C 1s peak at 284.8 eV. Figure 5a,b show that all samples exhibit intense characteristic peaks centered at approximately 486.9 eV (Sn $3d_{5/2}$) and 495.7 eV (Sn $3d_{3/2}$). These values are consistent with the standard binding energies of SnO_2, confirming that the material is predominantly in the SnO_2 phase. In contrast to pure SnO_2, Ni-SnO_2 samples show a systematic blue shift in the Sn 3d binding energies, indicating a reduced electron cloud density around Sn atoms [32]. This phenomenon may originate from charge redistribution induced by the effective doping of Ni^{2+} into the SnO_2 lattice, arising from valence-state and electronegativity differences between Ni^{2+} and Sn^{4+}. This redistribution weakens the shielding effect of the outer electrons of Sn ions, thereby increasing the Sn 3d binding energy. Among the samples, the 3 wt% Ni-SnO_2 sample exhibits the most pronounced peak shift, indicating the strongest modulation of its electronic structure. This electronic structure variation helps enhance surface activity and electron exchange efficiency, provideing a key physicochemical basis for the sensing properties of the 3 wt% Ni-SnO_2 sensor.

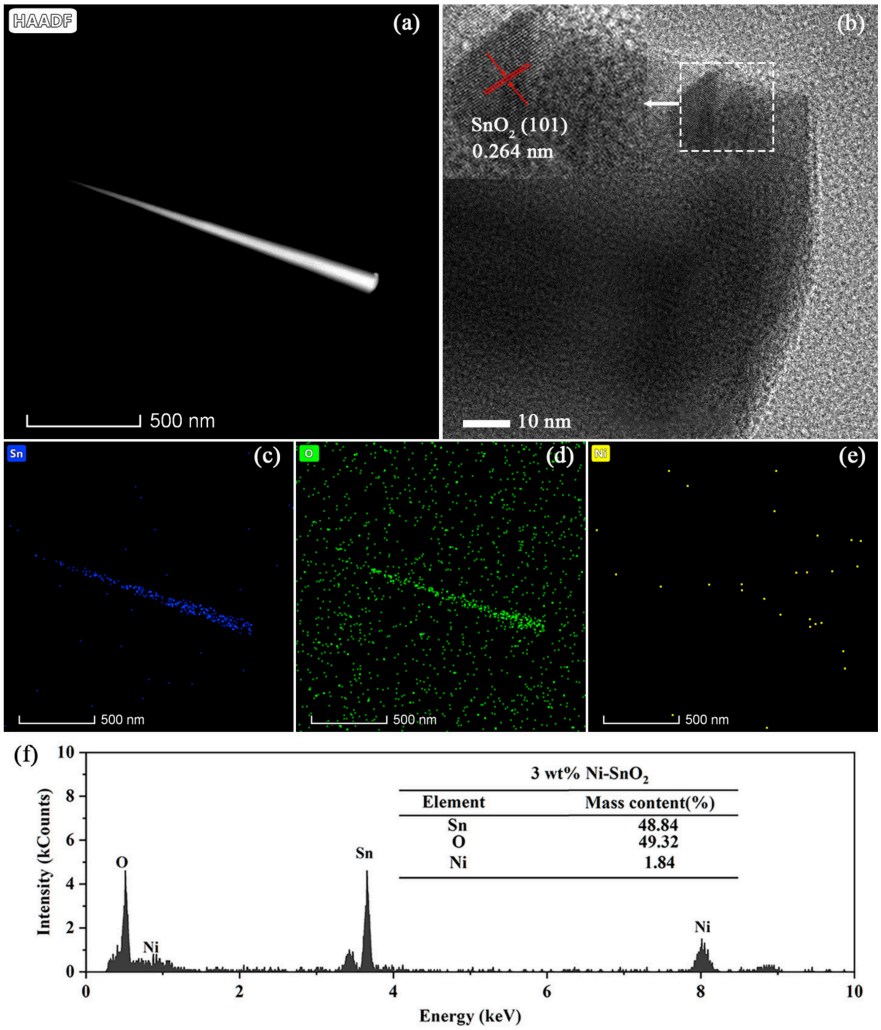

Figure 4. Results for 3 wt% Ni-SnO_2: (**a**) TEM, (**b**) HRTEM, (**c**–**e**) mapping (O, Sn, and Ni), and (**f**) EDS.

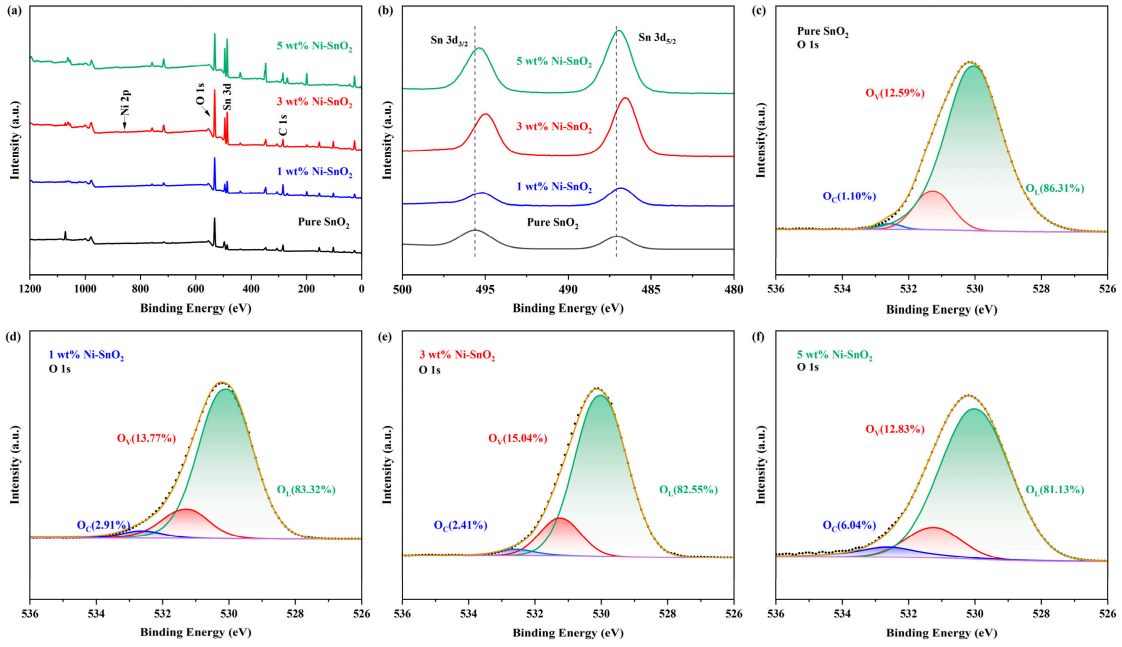

Figure 5. (**a**) Full-scan XPS spectra; (**b**) Sn 3d; (**c**) SnO_2; (**d**) 1 wt%; (**e**) 3 wt%; (**f**) 5 wt%.

The O 1s spectra were deconvoluted to distinguish different oxygen species for the pure SnO_2 and Ni-SnO_2 samples. Three characteristic components were observed in all cases, corresponding to lattice oxygen (O_L), oxygen vacancies (O_V) and chemisorbed oxygen (O_C) [33,34]. Figure 5c–f show the deconvoluted peaks at 530.2 eV, 531.8 eV and 532.4 eV as associated wth O_L, O_V and O_C, respectively. Quantitative analysis shows an oxygen vacancy concentration of 12.59% in pure SnO_2 (Figure 5c), which increases to 13.77% (Figure 5d), 15.04% (Figure 5e) and 12.83% (Figure 5f) for 1 wt% Ni-SnO_2, 3 wt% Ni-SnO_2, and 5 wt% Ni-SnO_2, respectively. The 1 wt% Ni-SnO_2 shows a lower oxygen vacancy concentration than the 3 wt% sample, likely due to the insufficient amount of Ni^{2+} available to substitute Sn^{4+} sites. At a doping level of 5 wt%, which exceeds the optimal ratio for this work, the oxygen vacancy concentration detected by XPS is notably reduced. Beyond the optimal doping threshold, point defects tend to recombine into electrically neutral defect clusters [35]. This aggregation process reduces the number of surface-exposed oxygen vacancy sites and simultaneously hinders charge carrier transport, thereby jointly contributing to the observed decrease in vacancy-related XPS signals. As highly active sites, these oxygen vacancies preferentially adsorb and activate environmental oxygen molecules to form chemisorbed species (e.g., O^- or O^{2-}), thereby markedly enhancing the surface reactivity toward target gases [36,37]. Therefore, an appropriate doped level can effectively achieve a balanced distribution of active sites; it provides a high density of reaction centers to promote gas-sensing reaction kinetics while avoiding adverse effects such as defect formation or Ni segregation that may occur at excessive doping levels.

As shown in Figure 6a, the Raman spectrum of the Ni-SnO_2 nanocomposite exhibits a strong peak at approximately 633 cm^{-1}, which is assigned to the A_1g vibrational mode of the rutile (cassiterite) crystal structure of SnO_2. In addition, two broad bands are observed at around 1360 cm^{-1} and 1592 cm^{-1}, corresponding to the D band and G band of carbonaceous species, respectively [38,39], indicating the presence of residual carbon from the synthesis process. It is worth noting that this residual carbon was not detected in the XRD patterns or EDS spectra. This is because the trace carbon exists in an amorphous state with an extremely low concentration, falling well below the semi-quantitative detection limits of XRD and EDS. However, due to the remarkably large Raman scattering cross-section of sp^2 carbonaceous structures, Raman spectroscopy exhibits extraordinary sensitivity, allowing the clear identification of even trace amounts of disordered carbon species [40]. For pure SnO_2 and Ni-SnO_2 samples with Ni doping levels of 1 wt%, 3 wt%, and 5 wt%, the characteristic peaks are located at 633.18, 631.28, 629.45, and 627.62 cm^{-1}, respectively. With increasing Ni doping, this peak systematically shifts to lower wavenumbers (red shift), indicating that the doping of Ni^{2+} causes lattice distortion and creates a high density of defects within the SnO_2 matrix. Among the doped samples, the 3 wt% Ni-SnO_2 maintains a strong peak intensity at 629.45 cm^{-1}, reflecting an optimal defect density and well-tailored lattice distortion. This moderate degree of lattice distortion and uniform defect distribution provides abundant active sites for gas and facilitates surface reactions, thereby significantly boosting the surface reaction kinetics. Consequently, the 3 wt% Ni-SnO_2 sample demonstrates the best catalytic performance and gas-sensing response toward hydrogen adsorption and oxidation.

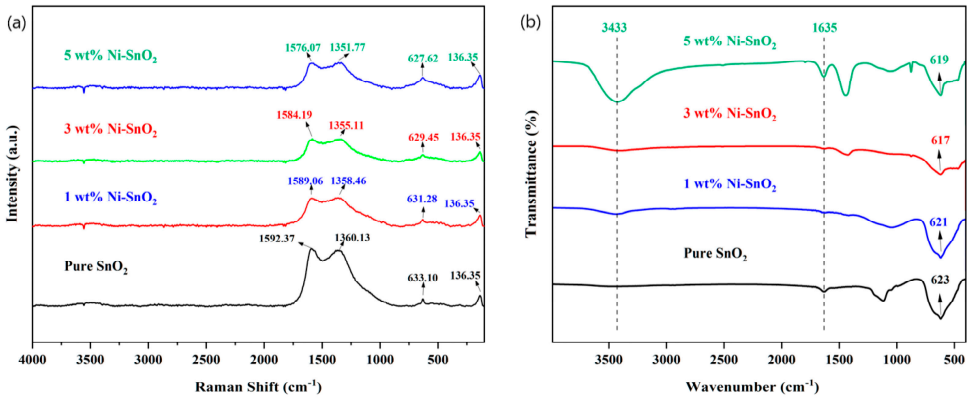

Figure 6. Spectroscopic characterization of all samples: (**a**) Raman spectra; (**b**) FT−IR spectra.

Following the analysis of molecular structure and surface chemistry, the samples were further investigated with FT-IR spectroscopy. According to Figure 6b, the spectral data indicate that pure SnO_2, as well as the Ni-SnO_2 samples with Ni loadings of 1 wt%, 3 wt%, and 5 wt%, all display a characteristic absorption peak near 633 cm^{-1}, assigned to the Sn-O lattice vibration mode of the rutile-structured SnO_2 [41]. This confirms that all samples retain the fundamental SnO_2 crystal framework. Notably, the Ni-doped samples exhibit distinct spectral features at 3438 cm^{-1} and 1635 cm^{-1}, which are assignable to the O-H elongation and H-O-H deformation vibrations, respectively [42,43]. The lattice defects and oxygen vacancy formation resulting from Ni^{2+} doping significantly enhance the surface activity and hydrophilicity of the material, thereby facilitating the adsorption of ambient water molecules. Among all doped samples, the 3 wt% Ni-SnO_2 sample exhibits the lowest intensity of these O-H related bands, while maintaining a sharp and well-defined Sn-O lattice peak. This observation indicates that the 3 wt% doping level achieves an optimal surface state: it generates sufficient oxygen vacancies to promote gas adsorption and surface reactions, while minimizing excessive surface hydroxylation, which would otherwise block active sites and impede charge transfer. Optimal doping generates a suitable density of oxygen vacancies and reactive surface sites, which act as primary centers for gas adsorption and surface reactions, enhancing surface kinetics and charge transport. Consequently, the 3 wt% Ni-SnO_2 sample exhibits a favorable structural and surface chemical configuration, including preserved morphology, increased defect concentration, and modified electronic structure, which may contribute to enhanced gas-sensing behavior as verified in the following sensing tests.

3.2. Gas-Sensing Performance

A systematic investigation was conducted to examine the correlation between the Ni doping level and the gas-sensing properties. The analysis encompassed gas-sensing data collected from a static testing system for four sensor variants: pure SnO_2 and 1, 3, and 5 wt% Ni-SnO_2. Figure 7a presents the comparative response behavior of the four sensors to 100 ppm H_2 across a range of operating temperatures. The results indicate that the gas-sensing performance improves gradually with increasing temperature and reaches its optimum at 310 °C. The response peaks at 310 °C, in clear contrast to its decline at higher temperatures, confirming this temperature as the optimal operating point. This temperature-dependent behavior can be explained as follows: at lower temperatures, gas molecules remain physically adsorbed on the material surface and cannot participate effectively in redox reactions. As the temperature increases, they acquire sufficient energy to undergo chemical adsorption and subsequent surface oxidation. However, when the temperature exceeds the optimum, excessively energetic gas molecules tend to desorb from the surface before undergoing reaction, consequently degrading the sensing signal [44]. At

310 °C, the 3 wt% Ni-SnO_2 sensor reaches a suitable balance between chemical adsorption and surface reaction kinetics, leading to a 110% response toward 100 ppm H_2. In contrast to pure SnO_2, Ni-SnO_2 devices show a significantly enhanced gas response. In this work, the optimal gas response is achieved at a Ni doping concentration of 3 wt%, due to the ideal balance between oxygen vacancies and lattice defects. This doping level creates an appropriate density of oxygen vacancies that act as active sites, efficiently adsorbing and activating H_2 molecule energy, but also suppress defect aggregation commonly observed at higher doping levels. The performance observed at 5 wt% Ni is likely attributable to a decrease in or saturation in oxygen vacancy concentration, which subsequently reduces carrier mobility and surface reactivity. Figure 7b illustrates that the sensor resistance increases as the temperature rises in air; however, the Ni-doped samples show significantly lower resistance than pure SnO_2. This reduction can be ascribed to the doping of Sn^{4+} with Ni^{2+}, which introduces oxygen vacancies to compensate for the charge imbalance [29]. Within a certain operating temperature range, the effect of oxygen adsorption and activation on the SnO_2 surface may outweigh the intrinsic increase in carrier transport, which can lead to an increase in baseline resistance with rising temperature. These vacancies act as electron donors, elevating the carrier concentration and thus reducing the baseline resistance. However, as the doping concentration rises, excessive Ni incorporates into the SnO_2 lattice, generating substantial lattice defects [45]. These defects perturb the periodic potential of the crystal structure, scattering charge carriers, and reduce their mobility, which ultimately results in an elevated sensor resistance.

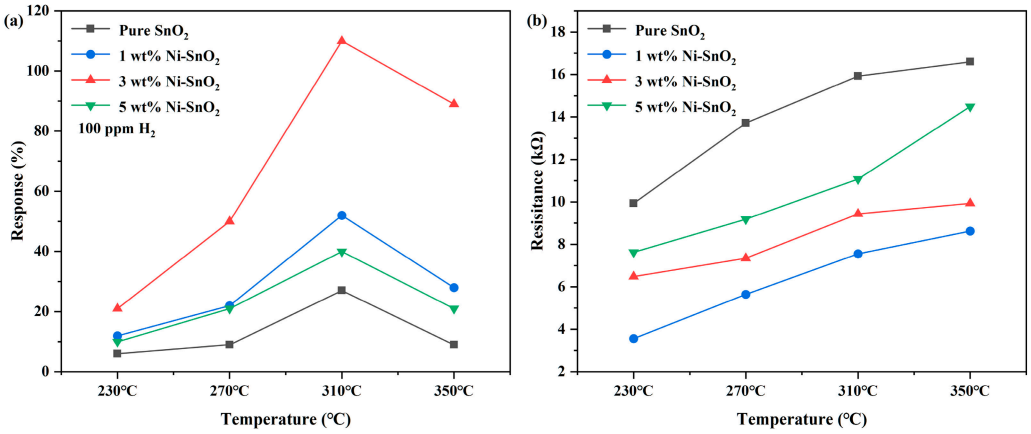

Figure 7. (**a**) Response values vs. operating temperature. (**b**) Resistance vs. operating temperature.

Figure 8 displays the dynamic response of SnO_2 and Ni-SnO_2 sensors (1, 3 and 5 wt%) to ppm-level H_2. As depicted in Figure 9, the response of each sensor increases monotonically with elevating H_2 concentration. Although the curves present a slight sub-linear curvature governed by a power-law relationship, they maintain a steady upward progression across the investigated concentration range while preserving stable baseline resistance in air. A comparison of the performance between pure and Ni-SnO_2 clearly shows that Ni doping significantly optimizes the sensor's detection limit and sensitivity. This demonstrates that Ni doping enhances sensor performance without compromising the structural stability of the SnO_2 matrix, thereby establishing a foundation for excellent reliability and repeatability. Furthermore, all four sensors achieve a detection limit of 500 ppb, while the 3 wt% Ni-SnO_2 sensor distinguishes itself with a detection limit of 100 ppb. The synergy of robust stability and high sensitivity provides a significant advantage for low-concentration hydrogen detection.

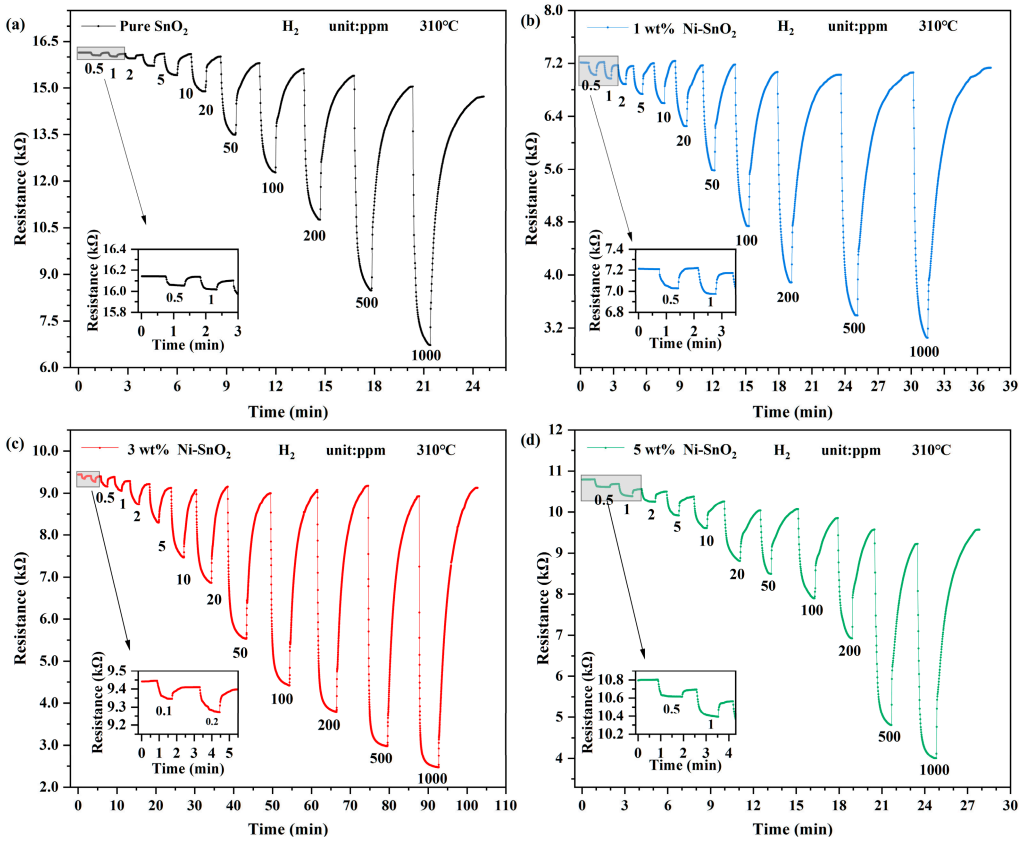

Figure 8. The response curves of (**a**) SnO_2, (**b**) 1 wt% Ni-SnO_2, (**c**) 3 wt% Ni-SnO_2, and (**d**) 5 wt% Ni-SnO_2.

Sensor repeatability was evaluated by cycling a specific gas concentration at 310 °C. Figure 10 shows the continuous five-cycle tests of SnO_2 and Ni-SnO_2 sensors with 1 wt%, 3 wt%, and 5 wt%, exposed to 5 ppm H_2 at 310 °C. The results demonstrate that the sensing signal variation across all four sensors remains below 2% during the cycling tests, demonstrating excellent repeatability and ensuring data authenticity. The high reproducibility enhances the sensor's measurement accuracy and operational reliability in practical detection. The average response values over the five cycles were 3%, 7%, 13% and 4% for pure SnO_2, 1 wt%, 3 wt%, and 5 wt% Ni-SnO_2, respectively. Although a slight increase in baseline resistance was observed, both the response and recovery times showed no significant degradation. Moreover, the baseline resistance quickly returned to its initial value after each cycle, with the resistance variation maintained within 5%, confirming the sensor's excellent reproducibility and long-term operational durability.

Based on its optimal overall sensing performance, the 3 wt% Ni-SnO_2 sensor was selected for further selectivity, response/recovery, humidity, and stability tests, and all measurements presented in Figure 11 were conducted with this sensor at 310 °C and 50% RH unless otherwise specified. Selectivity serves as a key performance indicator for evaluating a sensor's capability to accurately identify target gases in complex environments. As illustrated in Figure 11a, the study assessed the sensor's selectivity was assessed against a panel of common interfering gases (CO_2, CO, CH_4, and NH_3) at 100 ppm each. The findings reveal that the response to hydrogen is 5.7 times higher than that to NH_3, which exhibited the second-highest response. This excellent selectivity is primarily attributed to Ni doping on the SnO_2 surface, which creates specific catalytic sites for the synergistic promotion of hydrogen uptake and activation, thereby significantly enhancing surface reaction efficiency for hydrogenation. This high selectivity ensures the reliability of hydrogen detection. As illustrated in Figure 11b, the sensor signal exhibits a sharp drop during exposure to the

target gas, rapidly transitioning to a stable saturation state. When the environment is restored to clean air, the signal quickly returns to its initial level, indicating full recovery. Quantitative analysis yields a response time of 47 s (time to reach 90% of the steady-state response) and a recovery time of 71 s (time to return to 90% of the initial baseline) for 100 ppm H_2. These steep response slopes and complete baseline recovery indicate efficient gas adsorption–desorption kinetics and excellent reaction reversibility.

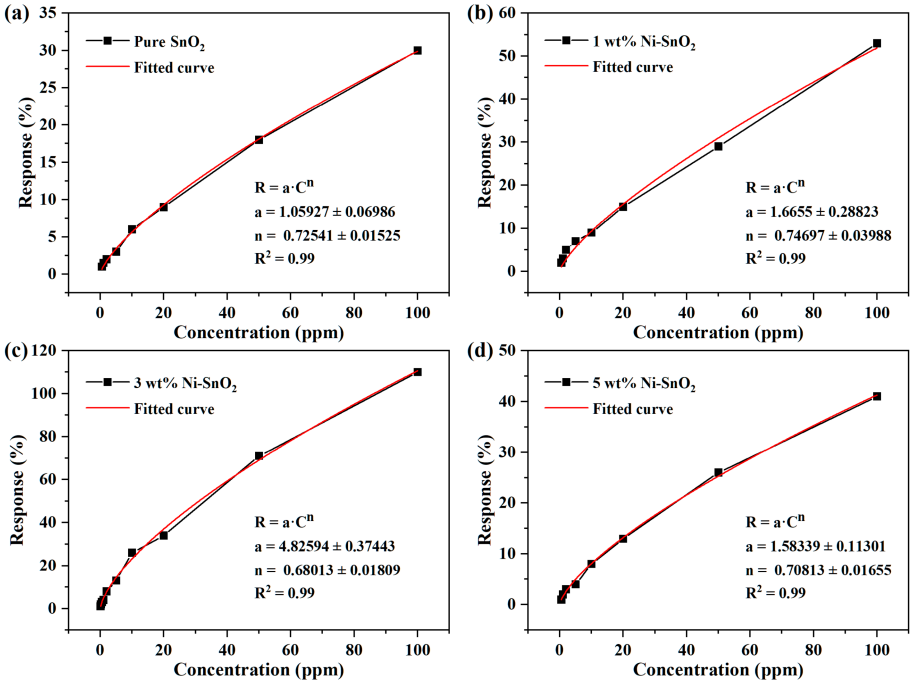

Figure 9. Response vs. concentration: (**a**) SnO_2, (**b**) 1 wt%, (**c**) 3 wt%, and (**d**) 5 wt% Ni-SnO_2.

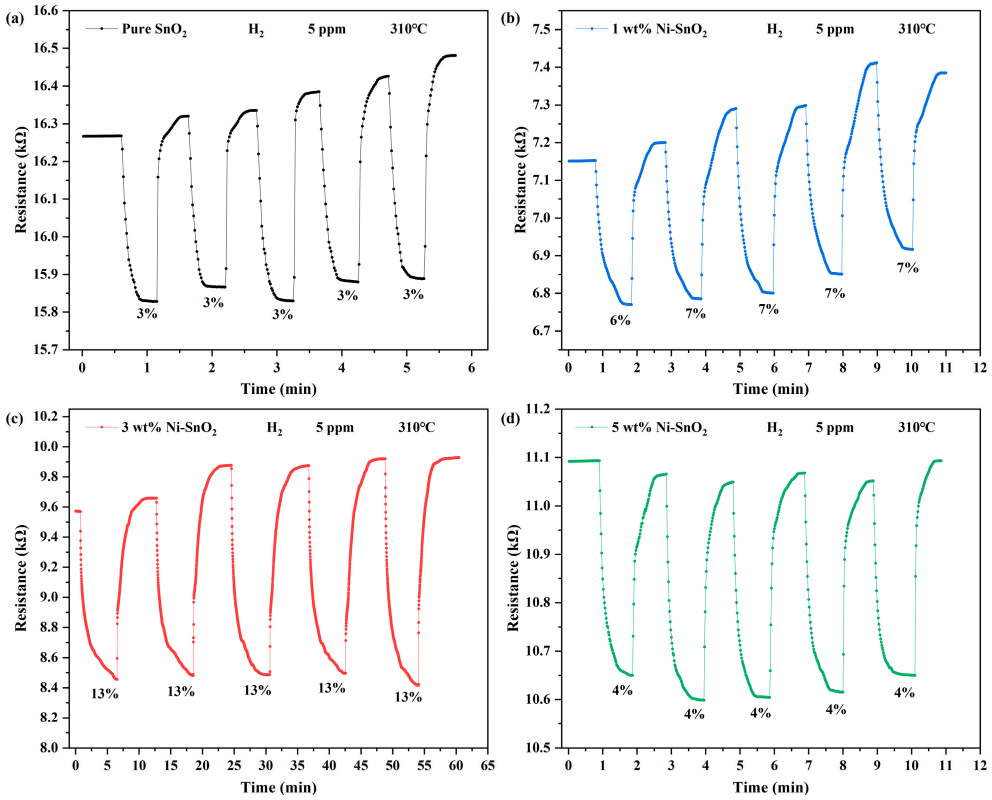

Figure 10. Five-cycle dynamic curves: (**a**) SnO_2, (**b**) 1 wt%, (**c**) 3 wt%, and (**d**) 5 wt%.

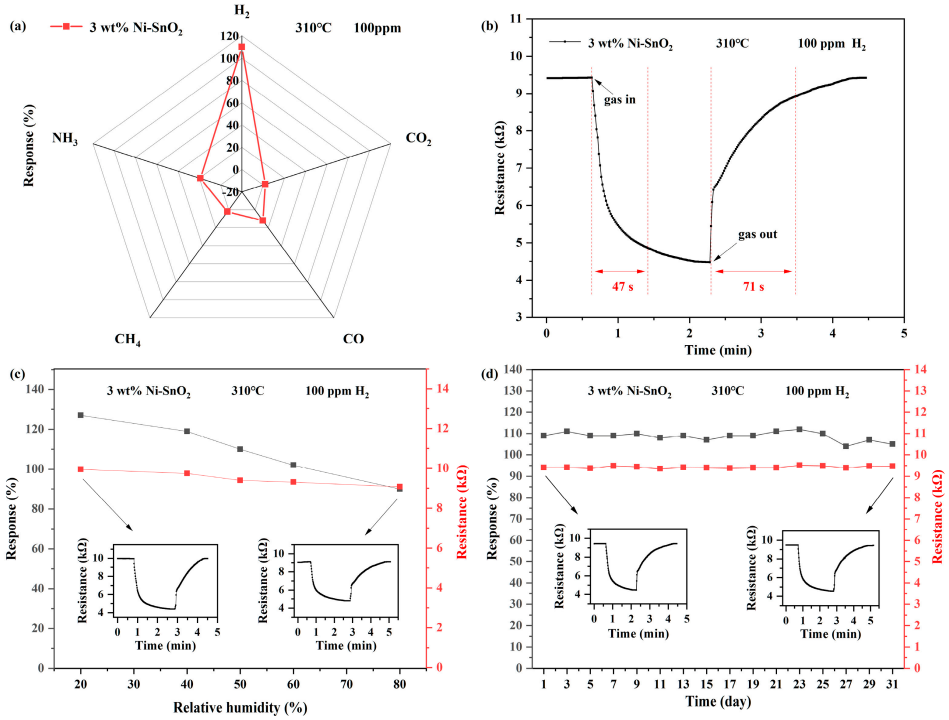

Figure 11. (**a**) Selective chart; (**b**) response−recovery curves; (**c**) response value and baseline resistance vs. relative humidity; (**d**) long−term stability (interpolated curves for days 1 and 31).

In practical applications, environmental humidity is a critical factor affecting the stability of metal oxide gas sensors. To systematically evaluate the sensor's moisture resistance, its response to a fixed hydrogen concentration was measured across a range of relative humidity levels (20% to 80% RH), as shown in Figure 11c. The results show a progressive decrease in sensor response from 127% at 20% RH to 90% at 80% RH, while the baseline drift remains well-controlled. Furthermore, the response and recovery times were measured and found to be largely unaffected by variations in humidity. These findings demonstrate the sensor's excellent moisture resistance, ensuring its detection accuracy and reliability in environments with fluctuating humidity. As shown in Figure 11d, the sensor was subjected to continuous monitoring and periodic testing over several weeks at 310 °C to investigate baseline resistance drift and its response to 100 ppm hydrogen. The results demonstrate no significant degradation in key performance parameters throughout the test cycle, and response fluctuations remain confined to a narrow range. The excellent long-term stability is attributed to the robust microstructure of the Ni-SnO_2 composite, which effectively suppresses grain coarsening at high operating temperatures and maintains the chemical stability of the gas-sensing interface. Table 1 shows a comprehensive contrast between the sensing performance of the developed Ni-SnO_2-based H_2 sensor and previously reported studies, a feature that distinguishes it even when its response magnitude is moderate compared with those of other sensors.

Table 1. Comparison of H_2 sensor performance.

Materials	Tem.	Method	Response (H_2)	Tres/Trec	LOD	Ref.
Pd/SnO_2	300 °C	VLS	56 at 100 ppm	22/164 s	1 ppm	[46]
Pd/SnO_2	130 °C	Electrospinning	53 at 500 ppm	44/350 s	5 ppm	[47]
MXene-SnO_2	400 °C	Hydrothermal	76% at 100 ppm	11/13 s	10 ppm	[48]
SnO_2	350 °C	CBD + CVD	271% at 100 ppm	2/29 s	1 ppb	[49]
WO_3/SnO_2	240 °C	Hydrothermal	12.06 at 1000 ppm	8/17 s	20 ppm	[50]
Ni-SnO_2	310 °C	AACVD	110% at 100 ppm	47/71 s	100 ppb	this work

3.3. Gas-Sensing Mechanism

The sensor constructed in this work consists of three main components: an alumina substrate, a forked gold electrode, and a Ni-doped SnO_2 sensing layer. The substrate offers mechanical support, the gold electrode facilitates electrical signal collection, and the Ni-SnO_2 thin film defines the gas-sensing characteristics, thereby governing the sensor's performance. The sensing mechanism is largely determined by the surface chemisorption of target gas molecules on the functional film. As demonstrated in Figure 12, the SnO_2 sensing layer consists of an assembly of nanorods. The structure presents a large specific surface area and high surface energy, which promote gas–solid reactions. In ambient air, oxygen molecules undergo facile adsorption onto the numerous dangling bonds and oxygen vacancies on the SnO_2 surface, thereby capturing free electrons from the conduction level [51]. The extraction of electrons from a near-surface electron depletion layer is associated with potential barriers. Given the n-type character of SnO_2, this results in a high baseline resistance [52]. This entire adsorption process stabilizes the sensor's electrical state against variations in oxygen partial pressure, ensuring consistent baseline resistance in air. In air:

$$O_2\ (gas) \rightarrow O_2\ (ads) \quad (1)$$

$$O_2\ (ads) + e^- \rightarrow {O_2}^-\ (ads)\ (<100\ ^\circ C) \quad (2)$$

$${O_2}^-\ (ads) + e^- \rightarrow 2O^-\ (ads)\ (100–300\ ^\circ C) \quad (3)$$

$$O^-\ (ads) + e^- \rightarrow O^{2-}\ (ads)\ (>300\ ^\circ C) \quad (4)$$

Upon exposure to hydrogen gas, the chemical reaction of H_2 molecules with the pre-adsorbed oxygen species on SnO_2 surface take place, thereby liberating the trapped electrons back into the conduction band, narrowing the electron depletion layer, and reducing the potential barrier height [53]. The magnitude of this resistance change is governed by the amount of pre-adsorbed oxygen involved in the reaction, which is positively correlated with hydrogen concentration. As the reaction proceeds, the resistance reaches equilibrium once H_2 and the adsorbed oxygen have fully reacted, generating a detectable response signal. Subsequent restoration to clean air allows oxygen molecules to re-adsorb onto the newly available active sites, causing the depletion layer and potential barrier to recover to their initial state, thereby completing the sensing cycle [54]. In H_2:

$$H_2\ (gas) \rightarrow 2H\ (ads) \quad (5)$$

$$4H\ (ads) + {O_2}^-\ (ads) \rightarrow 2H_2O + e^- \quad (6)$$

$$2H\ (ads) + O^-\ (ads) \rightarrow H_2O + e^- \quad (7)$$

$$4H\ (ads) + O^{2-}\ (ads) \rightarrow 2H_2O + 2e^- \quad (8)$$

Doping SnO_2 with Ni is a critical strategy for improving its performance as a gas sensor. Ni doping effectively modulates the electronic properties and surface characteristics of SnO_2, primarily through the following mechanisms that significantly improve H_2 sensing: First, the substitution of Sn^{4+} by Ni^{2+} introduces a charge compensation effect, generating numerous oxygen vacancy defects within the lattice [55]. Serving as highly active sites, these defects not only markedly improve the chemical adsorption capability for H_2 but also promote the activation of oxygen species at the material surface. Subsequently, H_2 molecules selectively undergo surface oxidation with these activated oxygen species at the vacancy sites, producing water molecules and liberating electrons back to the SnO_2 conduction band [56]. The reaction significantly modulates the concentration of charge carriers within the material, leading to a pronounced change in electrical conductivity and thereby

enabling highly sensitive and responsive hydrogen detection. Furthermore, the cation substitution defects introduced by Ni^{2+} effectively modify the SnO_2 band structure, shifting the Fermi level and creating localized energy states [57]. In summary, the defect state engineering achieved via Ni doping synergistically optimizes the surface activity, electron transport properties, and gas recognition capability of SnO_2 at the atomic scale, collectively contributing to its exceptional H_2 selectivity, high sensitivity and low detection limit.

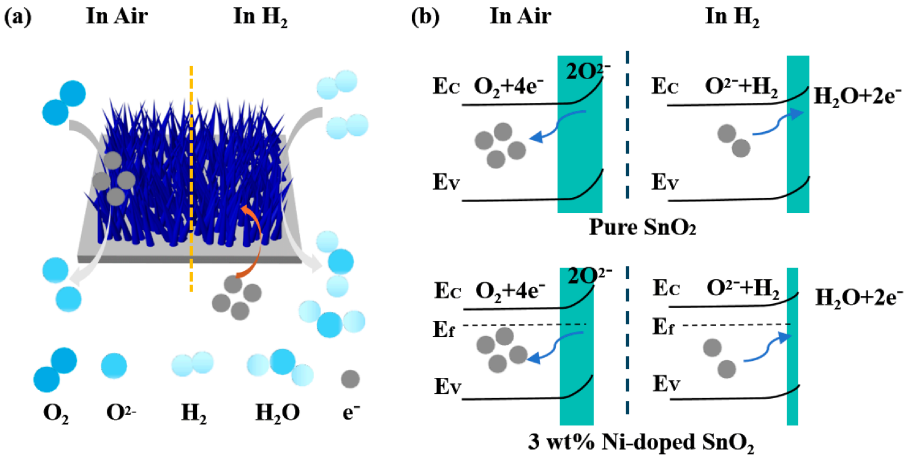

Figure 12. (**a**) Surface gas−sensing mechanism. (**b**) Energy bands.

4. Conclusions

In this work, we successfully fabricated Ni-doped SnO_2 nanorod films directly on planar electrodes using a single-step AACVD method. Compared with conventional multi-step fabrication techniques, this approach significantly simplifies the device preparation process while ensuring high material uniformity and structural reproducibility. Structural and spectroscopic characterizations (XRD, XPS, Raman, and FT-IR) consistently reveal that Ni doping effectively introduces abundant oxygen vacancies and lattice defects into the SnO_2 matrix. Among all tested ratios, the 3 wt% Ni-SnO_2 sample achieves a suitable balance between defect density and crystal stability, leading to substantially enhanced surface reactivity and charge transfer efficiency. Gas-sensing measurements demonstrate that the optimized 3 wt% Ni-SnO_2 sensor exhibits several key advantages: ultra-low detection limit of 100 ppb H_2, which is one order of magnitude lower than that of pristine SnO_2 and significantly outperforms many previously reported SnO_2-based hydrogen sensors; excellent selectivity, with a response to 100 ppm H_2 approximately 5.7 times higher than that to the next most responsive interfering gas (NH_3), ensuring reliable hydrogen detection in complex gas environments; good moisture resistance and long-term stability, with minimal baseline drift and no significant performance degradation over weeks of continuous operation, which is critical for practical applications; high repeatability, with less than 2% variation over five consecutive test cycles, confirming the robustness of the AACVD-grown nanostructures. Overall, this work establishes AACVD as a facile, scalable, and defect-engineering strategy for directly synthesizing high-performance metal oxide gas-sensing layers. The Ni-doped SnO_2 nanorod sensor developed herein offers a compelling combination of ultra-low detection limit, high selectivity, and long-term stability, positioning it as a promising candidate for low-concentration hydrogen leakage monitoring in future hydrogen energy infrastructure.

Author Contributions: P.C.: Writing—Original Draft. X.Z.: Validation. J.L.: Validation. X.L.: Writing—Review and Editing, Supervision, Resources, Project Administration, Funding Acquisition, and Conceptualization. M.C.: Formal Analysis. Q.W.: Writing—Review and Editing, Supervision,

Resources, Project Administration, Funding Acquisition, and Conceptualization. All authors have read and agreed to the published version of the manuscript.

Funding: This work is supported by the National Nature Science Foundation of China (62463003) and Hainan Provincial Natural Science Foundation of China (625MS051).

Institutional Review Board Statement: Not applicable.

Informed Consent Statement: Not applicable.

Data Availability Statement: The data can be obtained from the corresponding author.

Conflicts of Interest: The authors declare no competing financial interest.

References

1. Yang, X.-Y.; Shen, S.-M.; Yue, L.-J.; Gong, F.-L.; Xie, K.-F.; Wei, S.-Z.; Zhang, Y.-H. WO_3 decoration modulates the hydrogen spillover and oxygen activation over Pd/WO_3-SnO_2 nanotube for ultrafast hydrogen sensing. *Sens. Actuators B Chem.* **2025**, *441*, 138055–138065. [CrossRef]
2. Mei, H.; Peng, J.; Xu, D.; Wang, T. Low-Power Chemiresistive Gas Sensors for Transformer Fault Diagnosis. *Molecules* **2024**, *29*, 4625. [CrossRef] [PubMed]
3. Alenezy, E.K.; Sabri, Y.M.; Kandjani, A.E.; Korcoban, D.; Abdul Haroon Rashid, S.S.A.; Ippolito, S.J.; Bhargava, S.K. Low-Temperature Hydrogen Sensor: Enhanced Performance Enabled through Photoactive Pd-Decorated TiO_2 Colloidal Crystals. *ACS Sens.* **2020**, *5*, 3902–3914. [CrossRef] [PubMed]
4. Liu, X.; Sun, W.; Hu, X.; Chen, J.; Wen, Z. Self-powered H_2 generation implemented by hydrazine oxidation assisting hybrid electrochemical cell. *Chem. Eng. J.* **2023**, *474*, 145355–145365. [CrossRef]
5. Zhao, J.-T.; Du, Y.; Guo, X.-M. Mechanism of CO and H_2 sensitization and selectivity to tone up by Er-doped SnO_2 thin film. *Sens. Actuators B Chem.* **2025**, *442*, 138029–138043. [CrossRef]
6. Luo, Y.; Zhang, C.; Zheng, B.; Geng, X.; Debliquy, M. Hydrogen sensors based on noble metal doped metal-oxide semiconductor: A review. *Int. J. Hydrogen Energy* **2017**, *42*, 20386–20397. [CrossRef]
7. Abedzadeh, M.; Ranjbar, M.; Kameli, P. Fabrication of Pd-decorated tungsten oxide nanoflakes for hydrogen sensors via facile anodizing oxidation method. *Int. J. Hydrogen Energy* **2024**, *50*, 1325–1334. [CrossRef]
8. Sellam, M.; Rasheed, M.; Azizii, S.; Saidani, T. Improving photocatalytic performance: Creation and assessment of nanostructured SnO_2 thin films, pure and with nickel doping, using spray pyrolysis. *Ceram. Int.* **2024**, *50*, 20917–20935. [CrossRef]
9. Barala, S.; Kumar, A.; Kwoka, M.; Gupta, A.; Kumar, M. Spillover effect in Pd anchored NiO-ZnO nanostructures improves hydrogen gas sensor's performance. *Sens. Actuators B Chem.* **2025**, *433*, 137534–137544. [CrossRef]
10. Wu, J.; Gui, Y.; Tian, K.; Zhao, S.; Guo, D.; Guo, H.; Qin, X.; Qin, X.; Guo, Y. Ultrafast response and recovery in advanced H_2 sensing: Self-assembled fruit-leaf-like PdO/WO_3 nanostructures. *Sens. Actuators B Chem.* **2025**, *430*, 137339–137350. [CrossRef]
11. Zhang, S.; Li, J.; Zheng, Y.; Zhang, B.; Luo, N.; Wang, Y. PtPd alloy-enhanced cube In_2O_3 for hydrogen sensing: Low detection limits and reduced operating temperatures. *Appl. Surf. Sci.* **2025**, *710*, 163926–163937. [CrossRef]
12. Kumar, R.; Mamta; Kumari, R.; Singh, V.N. SnO_2-Based NO_2 Gas Sensor with Outstanding Sensing Performance at Room Temperature. *Micromachines* **2023**, *14*, 728. [CrossRef] [PubMed]
13. El-Maghraby, E.M.; Qurashi, A.; Yamazaki, T. Synthesis of SnO_2 nanowires their structural and H_2 gas sensing properties. *Ceram. Int.* **2013**, *39*, 8475–8480. [CrossRef]
14. Jeong, J.; Lee, J.-W.; Lee, J.; Shin, K.; Lee, H.-S.; Lee, W. Highly stable and reversible hydrogen sensors using Pd-coated SnO_2 nanorods and an electrode–substrate interface as a parallel conduction channel. *Sens. Actuators B Chem.* **2023**, *394*, 134350. [CrossRef]
15. Palanisamy, B.; A, G.; Harish, S.K.; Mani, K.M.; Archana, J.; Mani, N. Hierarchical SnS_2/SnO_2 Heterostructures for Synergistic NO_2 Sensing under Ambient Conditions. *ACS Appl. Nano Mater.* **2025**, *8*, 17042–17051. [CrossRef]
16. Chen, Y.; Yuan, T.; Shen, B.; Zhang, W.; Xu, J.; Wu, M. Atom-thin SnO_2 sheets composed with g-C_3N_4 matrix as HCHO sensor with high thermal stability. *Ceram. Int.* **2024**, *50*, 42518–42527. [CrossRef]
17. Güney, H.; İskenderoğlu, D.; Karadenïz, S.M.; Güldüren, M.E.; Saritaş, S. Zn-doping effects on ultrasonically spray-pyrolyzed CuO thin films: Interplay between material properties and gas sensing performance. *Ceram. Int.* **2025**, *51*, 54928–54937. [CrossRef]
18. Patil, S.B.; Patil, G.E.; Dalal, P.V. Enhanced gas sensing performance of ZnO and Pt-doped ZnO nanostructured films by chemical spray pyrolysis. *Surf. Interfaces* **2024**, *54*, 105173–105181. [CrossRef]
19. Jang, B.-H.; Landau, O.; Choi, S.-J.; Shin, J.; Rothschild, A.; Kim, I.-D. Selectivity enhancement of SnO_2 nanofiber gas sensors by functionalization with Pt nanocatalysts and manipulation of the operation temperature. *Sens. Actuators B Chem.* **2013**, *188*, 156–168. [CrossRef]

20. Zhang, X.-Y.; Ren, Q.; Wang, C.; Zhu, L.; Ding, W.-J.; Cao, Y.-Q.; Li, W.-M.; Wu, D.; Li, A.-D. Atomic layer deposited SnO_2/ZnO composite thin film sensors with enhanced hydrogen sensing performance. *Appl. Surf. Sci.* **2023**, *639*, 157973–157981. [CrossRef]
21. Li, J.; Zheng, M.; Yang, M.; Zhang, X.; Cheng, X.; Zhou, X.; Gao, S.; Xu, Y.; Huo, L. Three-in-one Ni doped porous SnO_2 nanorods sensor: Controllable oxygen vacancies content, surface site activation and low power consumption for highly selective NO_2 monitoring. *Sens. Actuators B Chem.* **2023**, *382*, 133550–1133559. [CrossRef]
22. Wang, Q.; Ma, Y.; Yang, T.; Jiao, Y.; Lang, D.; Huang, Y.; Cheng, L.; Wang, T. Triggered new active sites and fast charge transfer in TiO_2@N-doped MoS_2 for ppb-level ethanol detection at low temperatures via heterogeneous interface construction. *Ceram. Int.* **2025**, *51*, 43836–43847. [CrossRef]
23. Gu, G.; Zhou, W.; Kong, D.; Gao, Y.; Liao, C.; Yu, N.; Xu, J.; Han, J.; Wang, Y.; Lu, G. Synergistic surface spin polarization in W-doped Co_3O_4 enables high-performance TEA sensing. *Sens. Actuators B Chem.* **2026**, *449*, 139081–139093. [CrossRef]
24. Guo, W.; Yi, J.; Luo, X.; Wang, S.; Zhang, J.; Zhang, H. The Ni-doped SnS_2/SnO_2 hexagonal nanosheets with enhanced gas sensing performance for effective detection of n-butanol. *Mater. Chem. Phys.* **2025**, *346*, 131406–131417. [CrossRef]
25. Wang, L.; Shen, Y.; Jiao, Z.; Xu, X.; Xiang, J.; Huang, S.; Lu, T.; Hou, X. Sensitive hydrogen sensing using SnO_2 enabled by single-layer graphene composites. *J. Mater. Sci. Mater. Electron.* **2025**, *36*, 263. [CrossRef]
26. Hu, K.; Wang, F.; Shen, Z.; Liu, H.; Xiong, J. Ternary heterojunctions synthesis and sensing mechanism of Pd/ZnO–SnO_2 hollow nanofibers with enhanced H_2 gas sensing properties. *J. Alloys Compd.* **2021**, *850*, 156663–156675. [CrossRef]
27. Zhao, S.; Shi, J.; Yan, C.; Ding, X.; Wang, W.; Liu, W.; Shen, Y.; Zhao, Q. Preparation of SnO_2 film on porous diatomite-based substrate by AACVD for high-performance H2 sensing. *Ceram. Int.* **2025**, *51*, 18563–18572. [CrossRef]
28. Roguai, S.; Djelloul, A. Structural, morphological, optical and electrical properties of Ni-doped SnO_2 thin films by pneumatic spray pyrolysis method. *Bull. Mater. Sci.* **2022**, *45*, 227–236. [CrossRef]
29. Das, S.; Girija, K.G.; Debnath, A.K.; Vatsa, R.K. Enhanced NO_2 and SO_2 sensor response under ambient conditions by polyol synthesized Ni doped SnO_2 nanoparticles. *J. Alloys Compd.* **2021**, *854*, 157276–157286. [CrossRef]
30. Zhang, B.; An, X.; Zhang, S.; Wang, C.; Zhao, Z.; Bala, H.; Zhang, Z. Two-step growth of core-shell TiO_2/SnO_2 nanorod arrays on FTO and its application in gas sensor. *J. Alloys Compd.* **2023**, *946*, 169382–169392. [CrossRef]
31. Chen, L.; Liu, C.-C.; Yang, T.-Y.; Liu, Y.-X.; Zhang, Y.-Q.; Guo, Z. Porous SnO_2 Nanofibers Embedded with Hollow Hetero-Metal Oxide Nanospheres for Enhanced Gas Sensing. *ACS Appl. Mater. Interfaces* **2025**, *17*, 55097–55106. [CrossRef] [PubMed]
32. Mohan, V.K.; R, C.P.; N, A.; Jha, S.N.; Bhattacharyya, D.; John, T.T. Ni-doped SnO_2 nanoparticles: Structural insights and magnetic behavior via X-ray absorption spectroscopy. *Mater. Sci. Semicond. Process.* **2025**, *192*, 109415–109425. [CrossRef]
33. Song, B.-Y.; Li, C.; Lv, M.-S.; Zhang, X.-F.; Deng, Z.-P.; Xu, Y.-M.; Huo, L.-H.; Gao, S. Biotemplate-inherited porous SnO_2 monotubes with oxygen vacancies for ultra-high response and fast detection of nitric oxide at low temperature. *Sens. Actuators B Chem.* **2023**, *387*, 133811–133820. [CrossRef]
34. Xin, C.; Zhao, L.; Xing, Y.; Zhang, H.; Yu, C.; Wei, Z.; Fei, T.; Liu, S.; Zhang, H.; Zhang, T. An in situ exsolution strategy to prepare metallic Sn modified SnO_2 with oxygen vacancies for ppb-level NO_2 detection. *Sens. Actuators B Chem.* **2024**, *419*, 136232–136243. [CrossRef]
35. Ciftyurek, E.; Li, Z.; Schierbaum, K. Adsorbed Oxygen Ions and Oxygen Vacancies: Their Concentration and Distribution in Metal Oxide Chemical Sensors and Influencing Role in Sensitivity and Sensing Mechanisms. *Sensors* **2022**, *23*, 29. [CrossRef] [PubMed]
36. Ding, Y.; Chen, Y.; Wang, M. Oxygen vacancy-dependent humidity sensing performance induced by Si doping on SnO_2 nanoparticles. *Micro Nanostruct.* **2024**, *192*, 207890–207903. [CrossRef]
37. Wang, L.; Ma, S.; Xu, X.; Li, J.; Yang, T.; Cao, P.; Yun, P.; Wang, S.; Han, T. Oxygen vacancy-based Tb-doped SnO_2 nanotubes as an ultra-sensitive sensor for ethanol detection. *Sens. Actuators B Chem.* **2021**, *344*, 130111–130122. [CrossRef]
38. Sao, D.; Mandal, R.; Mahato, S.; Das, P.S.; Roy, G.; Panda, B.; Dhak, D.; Kuiri, P.K.; Mukherjee, B.; Nath, R. Sonochemically synthesized integrated silver-tin oxide nanostructure for enhanced photocatalytic applications. *Phys. B Condens. Matter* **2025**, *715*, 417548–417560. [CrossRef]
39. Le, Y.T.-H.; Yoo, H.; Lee, H.; Park, S.; Jeon, K.-J. The impact of carbonaceous and inorganic aerosols on haze dynamics: Insights from size-resolved analysis. *Atmos. Environ.* **2025**, *362*, 121590–121600. [CrossRef]
40. Kuzume, A.; Ozawa, M.; Tang, Y.; Yamada, Y.; Haruta, N.; Yamamoto, K. Ultrahigh sensitive Raman spectroscopy for sub-nanoscience: Direct observation of tin oxide clusters. *Sci. Adv.* **2019**, *5*, 6455–6462. [CrossRef]
41. Zhou, F.Y.; Hong, B.; Xu, J.C.; Han, Y.B.; Jin, H.X.; Jin, D.F.; Zeng, Y.X.; Peng, X.L.; Ge, H.L.; Wang, X.Q. Synthesis and enhanced formaldehyde gas-sensing performance of mesoporous SnO_2 nanospheres doped with trivalent metal-cations. *J. Mater. Sci.* **2023**, *58*, 3670–3686. [CrossRef]
42. Zhou, H.; Li, Y.; Du, Q.; Pi, X.; Zhang, J.; Wang, X.; Chen, B.; Yin, L.; Zhang, Y.; Li, Y.; et al. Preparation and characterization of zirconium-based metal-organic skeleton composite sodium alginate@SiO_2 and its adsorption on methylene blue solution in water. *Int. J. Biol. Macromol.* **2025**, *304*, 140916–140932. [CrossRef] [PubMed]
43. Yu, J.-J.; Wang, L.; Xue, Z.-L. Preparation of Mo_2C by the temperature-programmed reaction between h-MoO_3 and CO. *Ceram. Int.* **2023**, *49*, 33135–33146. [CrossRef]

44. Lin, Z.; Li, N.; Chen, Z.; Fu, P. The effect of Ni doping concentration on the gas sensing properties of Ni doped SnO_2. *Sens. Actuators B Chem.* **2017**, *239*, 501–510. [CrossRef]
45. Hu, J.; Wang, T.; Wang, Y.; Huang, D.; He, G.; Han, Y.; Hu, N.; Su, Y.; Zhou, Z.; Zhang, Y.; et al. Enhanced formaldehyde detection based on Ni doping of SnO_2 nanoparticles by one-step synthesis. *Sens. Actuators B Chem.* **2018**, *263*, 120–128. [CrossRef]
46. Cai, Z.; Park, S. Synthesis of Pd nanoparticle-decorated SnO_2 nanowires and determination of the optimum quantity of Pd nanoparticles for highly sensitive and selective hydrogen gas sensor. *Sens. Actuators B Chem.* **2020**, *322*, 128651–128665. [CrossRef]
47. Hu, K.; Wang, F.; Liu, H.; Li, Y.; Zeng, W. Enhanced hydrogen gas sensing properties of Pd-doped SnO_2 nanofibres by Ar plasma treatment. *Ceram. Int.* **2020**, *46*, 1609–1614. [CrossRef]
48. Chen, Q.; Zhang, Y.; Tang, M.; Wang, Z.; Zhang, D. A fast response hydrogen sensor based on the heterojunction of MXene and SnO_2 nanosheets for lithium-ion battery failure detection. *Sens. Actuators B Chem.* **2024**, *405*, 135229–135240. [CrossRef]
49. Li, Y.; Pang, C.; Xue, L.; Li, X.; Wang, Q. Chemiresistive SnO_2-based hydrogen sensor fabricated by chemical bath deposition and chemical vapor deposition. *Sens. Actuators B Chem.* **2025**, *433*, 137543–137553. [CrossRef]
50. Hu, J.; Xu, T.; Jin, L.; Hong, Z.; Song, Z.; Kong, Z.; Li, H.-j.; Liao, Q.; Xu, J.; Li, G.; et al. Two-Dimensional Hybrid SnO_2@WO_3 Nanosheets Synthesized by Polyoxometallate Cluster–Nucleus Coassembly for Highly Efficient H2 Detection. *ACS Sens.* **2025**, *10*, 7810–7819. [CrossRef] [PubMed]
51. Al-Hashem, M.; Akbar, S.; Morris, P. Role of Oxygen Vacancies in Nanostructured Metal-Oxide Gas Sensors: A Review. *Sens. Actuators B Chem.* **2019**, *301*, 126845–126869. [CrossRef]
52. Krishna, K.G.; Parne, S.; Pothukanuri, N.; Kathirvelu, V.; Gandi, S.; Joshi, D. Nanostructured metal oxide semiconductor-based gas sensors: A comprehensive review. *Sens. Actuators A Phys.* **2022**, *341*, 113578. [CrossRef]
53. Amiri, V.; Roshan, H.; Mirzaei, A.; Neri, G.; Ayesh, A.I. Nanostructured Metal Oxide-Based Acetone Gas Sensors: A Review. *Sensors* **2020**, *20*, 3096. [CrossRef] [PubMed]
54. Zheng, X.; Fan, H.; Wang, H.; Yan, B.; Ma, J.; Wang, W.; Yadav, A.K.; Dong, W.; Wang, S. ZnO–SnO_2 nano-heterostructures with high-energy facets for high selective and sensitive chlorine gas sensor. *Ceram. Int.* **2020**, *46*, 27499–27507. [CrossRef]
55. Sun, J.; Yin, G.; Cai, T.; Yu, W.; Peng, F.; Sun, Y.; Zhang, F.; Lu, J.; Ge, M.; He, D. The role of oxygen vacancies in the sensing properties of Ni substituted SnO_2 microspheres. *RSC Adv.* **2018**, *8*, 33080–33086. [CrossRef] [PubMed]
56. Li, W.-T.; Zhang, X.-D.; Guo, X. Electrospun Ni-doped SnO_2 nanofiber array for selective sensing of NO_2. *Sens. Actuators B Chem.* **2017**, *244*, 509–521. [CrossRef]
57. Sedky, A.; Hakamy, A.; Afify, N.; Bouhmaidi, S.; Setti, L.; Hamad, D.; Abd-Elnaiem, A.M. Comparative investigation of structural, photoluminescence, and magnetic characteristics of $M_xSn_{1-x}O_y$ nanocomposites. *Appl. Phys. A* **2023**, *129*, 669–686. [CrossRef]